Research Article Vol. 57, No. 27 / 20 September 2018 / Applied Optics 8065

applied optics

Determination of vibration amplitudes from binary phase patterns obtained by phase-shifting time-averaged speckle shearing interferometry

Murielle Kirkove,[1,*] Stéphanie Guérit,[2,4] Laurent Jacques,[2] Christophe Loffet,[3] Fabian Languy,[1] Jean-François Vandenrijt,[1] and Marc Georges[1]

[1]Centre Spatial de Liège, Université de Liège, Liege Science Park, B-4031 Angleur (Liège), Belgium
[2]ISPGroup/ICTEAM, Université catholique de Louvain, B-1348 Louvain-la-Neuve, Belgium
[3]V2i S.A., Liege Science Park, B-4031 Angleur (Liège), Belgium
[4]e-mail: stephanie.guerit@uclouvain.be
*Corresponding author: M.Kirkove@ulg.ac.be

Received 25 May 2018; revised 15 August 2018; accepted 23 August 2018; posted 24 August 2018 (Doc. ID 332462); published 19 September 2018

Speckle shearing interferometry (shearography) is a full-field strain measurement technique that can be used in vibration analysis. In our case, we apply a method that combines the time-averaging and phase-shifting techniques. It produces binary phase patterns, where the phase changes are related to the zeroes of a Bessel J_0 function, typical of time-averaging. However, the contrast and resolution are better compared to traditional time-averaging. In a previous paper, we have shown that this is particularly useful in vibration testing performed under industrial conditions, because fringe patterns are noisier than in quiet laboratory environments. This paper goes a step further in proposing a processing method for estimating the vibration amplitude, for helping non-experts to identify vibration modes. Since shearography measures the spatial derivative of displacement, spatial integration is required. Prior to that, different processes like denoising, binarization, automated nodal line detection, and amplitude assignment are applied. We analyze the performance of the method on synthetic and experimental data, in the function of noise level and fringes density. Results on data acquired in an industrial environment illustrate the good performances of the proposed method.

OCIS codes: (120.6160) Speckle interferometry; (120.7280) Vibration analysis; (100.2650) Fringe analysis.

https://doi.org/10.1364/AO.57.008065

1. INTRODUCTION

Interferometric techniques, such as analog holographic interferometry (HI) [1], digital HI [2], electronic speckle pattern interferometry (ESPI), sometimes called total variation (TV) holography [1,3], and speckle shearing interferometry (shearography) [4], are contactless optical techniques used in the field of non-destructive testing for measuring displacement fields or strains. They can also be used for vibration analysis [1,4], with the ultimate goal to provide the vibration amplitude of mode shapes appearing at resonance frequencies. All techniques use a laser that illuminates the object under vibration. In all cases, except shearography, one part of the laser beam is extracted (so-called reference beam) and directly impinges the recording device, where it interferes with the light reflected by the object (so-called object beam), forming a hologram or specklegram in the function of the technique considered. In shearography, there is no reference beam: one records the interference pattern between a speckle object wavefront and itself laterally shifting through an optical shearing device [4]. Such interference patterns, called shearograms, are recorded at different instants during object deformation. The numerical difference between two shearograms gives rise to an interferogram that allows for observing the derivative of the full-field displacement of the object along the optical shear direction. Because of its self-referenced optical scheme, shearography is less sensitive to environmental disturbances than other techniques using a reference beam. It is the only one usable in highly unstable environments. It has, hence, become an important measurement tool outside the optics laboratory [5–7].

For observation of vibration modes close to resonance, all interferometry techniques (including shearography) have been demonstrated through various configurations. The best-known is time-averaging (TA) [8–10], in which interference patterns (holograms, specklegrams, or shearograms) are recorded over an integration time much longer than the object vibration period. Assuming the object is sinusoidally excited, the intensity images

show Bessel-type interference fringes (Besselograms) with a maximum of intensity at the vibration nodes and a rapidly decreasing contrast from the nodes to antinodes. Intense researches are carried out since the invention of TA interferometry for retrieving the vibration amplitude through phase computation methods. For applying the latter, phase variation has to be introduced, e.g., by moving the phase of the reference beam at the frequency of object excitation, as demonstrated in TA [11]. This allowed for the use of the popular temporal phase-shifting (TPS) in TA [12]. However, TPS is adapted to sinusoidal fringe patterns captured by all of the above cited interferometric techniques. Applying it to TA is not straightforward because of the disparity between Bessel and sinusoidal functions [12]. Most works carried out in the field made use of reference wave modulation, together with various strategies for correcting such disparity in view of vibration amplitude determination [13–16]. Other techniques were applied to TA, like amplitude variation of the reference frame [17] and introduction of a spatial carrier [18]. Simpler implementations with single frame analysis based on Hilbert transform [19] or with further improvements were also considered [20,21]. Another class of interferometry methods for vibration analysis avoids TA and Bessel fringes and is based on the stroboscopic real-time method [10,22]. It assumes shuttering the object illumination in synchronization with the excitation. For that, it requires additional synchronized shutter, chopper, or deflection of the beams. This is necessary to illuminate the scene only when the object is at its maximum of displacement, which temporarily freezes its movement. As a result, the holograms, specklegrams, or shearograms can be recorded at rest and during vibration. TPS can be applied for computing phases in each state, and the phase difference shows interferograms that can be easily evaluated in the same way as for non-vibrating objects [23]. This advantage is counterbalanced by an important loss of light due to the stroboscopic operation, which limits the applicability to small objects. Also, the nodal line corresponding to a zero displacement (e.g., at clamping points) cannot be determined by stroboscopic techniques, contrary to TA-based configurations.

An interesting alternative also combines the TA technique with TPS and is referred to here as the phase-shifting time-averaged (PSTA) method [24–26]. It has a big advantage over the two classes of techniques cited previously: PSTA does not make use of a phase-shifter included in the excitation loop for precise control of the phase. Instead, it uses the simple principle of phase-shifting in one of the two beams, without any specific synchronization to the object excitation. Therefore, a basic interferometric setup (i.e., not specifically developed for vibrations) can be used. We already presented developments and the application of PSTA shearography for mode shapes visualization in industrial environments [27,28]. However, the method provides binary phase fringes. We showed that it is advantageous compared to Besselograms, where modal displacements are important. In particular, the fringe contrast is found to be better in the binary phase patterns of PSTA compared to the contrast of other traditional TA-based configurations.

Our previous works [27,28] only proposed qualitative results, sufficient for identification of mode shapes, e.g., through comparison with calculated ones. The final purpose of our work is to provide images from shearographic acquisitions that will help non-experts to identify the most important vibration modes in strain tests at frequencies below 10 kHz. Our work departs from other ones in the fact that, because we use shearography, we need integration of patterns. With the integration process being impacted by noise, pre-processing was needed, and it led to different processing steps presented in the paper, up to the determination of vibration amplitude.

The paper is structured as follows. Section 2 reviews the basics of shearography PSTA. Two experimental data sets are introduced in Section 3. Section 4 describes the pre-processing, which consists of phase rotation and denoising. Their performance will be assessed on both synthetic and experimental data. In Section 5, we describe the main processing, which reconstructs the displacement and vibration amplitude maps. The section also includes its qualitative evaluation on real data.

2. BASICS OF SHEAROGRAPHY PSTA METHOD

As illustrated in Fig. 1, shearography acquisition proceeds by illuminating an object under vibration with a laser. Light scattered by the object surface is observed by a camera through a shearing device of the Michelson interferometer type. The latter consists of a beam-splitter cube (BS) with mirrors M_1 and M_2 placed in the transmitted and reflected arms of the BS, respectively. This assembly splits the object image into two parts that are retro-reflected by two mirrors before entering a camera with its objective lens (OL).

If one of the mirrors is slightly tilted (e.g., M_2 in Fig. 1), both reflected images I_{o1} and I_{o2} appear transversally shifted from the other in the direction e_s. The shift is called the shear displacement, and the direction e_s is the shear direction. In the overlapping region (see gray area in Fig. 1), interference occurs, giving rise to the shearogram.

During vibration, the instantaneous intensity $I_{\text{inst}}(t)$ in each pixel of the camera plane is given by

$$\begin{cases} I_{\text{inst}}(t) = I_{o1} + I_{o2} + I_m \cos(\phi + \delta(t)) \\ I_m = 2(I_{o1} I_{o2})^{1/2} \end{cases}, \tag{1}$$

where I_m is the modulation intensity, ϕ is the phase difference between both interfering images, and $\delta(t)$ is the optical phase variation due to vibration displacement, which is given by

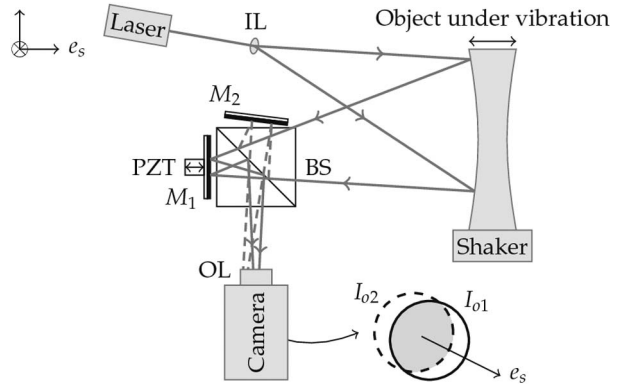

Fig. 1. Shearography setup and resulting shifted images with overlap in gray.

$$\delta(t) = \delta_A \sin(\omega t), \tag{2}$$

with δ_A as the amplitude of the optical phase variation and ω as the cyclic frequency of vibration. Our method assumes TA of the instantaneous intensity profile $I_{\text{inst}}(t)$ obtained by recording shearograms over a time longer than the period of vibration $2\pi/\omega$. The resulting pattern can be described as [28]

$$I = I_{o1} + I_{o2} + I_m \cos(\phi) J_0(\delta_A), \tag{3}$$

where J_0 is the zeroth-order Bessel function of the first kind.

At any time, the phase difference $\Delta\phi$ between the phase ϕ and a reference phase ϕ_r, related to the resting state (i.e., without vibration), can be computed using the phase-shifting technique [29]. This consists of acquiring a set of shearograms with an additional known phase shift between each capture. For that purpose, a piezoelectric translator (PZT) moves mirror M_1 to produce the phase shift (see Fig. 1). Usually, we use the four-step algorithm with a phase shift $\Delta\phi_s$ of $\pi/2$. The four acquisitions are expressed as

$$I_k = I_{o1} + I_{o2} + I_m \cos(\phi + k\Delta\phi_s) J_0(\delta_A) \tag{4}$$

for $k \in \{0, 1, 2, 3\}$. At the resting state, δ_A is zero so that $J_0(\delta_A)$ is one (see Fig. 2), and ϕ_r is computed from the four acquisitions [29] by

$$\phi_r = \tan^{-1}((I_3 - I_1)/(I_0 - I_2)). \tag{5}$$

When vibration occurs, $J_0(\delta_A)$, the multiplicative term in Eq. (4), takes any real value. Phase ϕ is undefined when $J_0(\delta_A)$ is zero and, otherwise, is computed on each pixel by

$$\phi = \phi_r + \begin{cases} 0 & \text{if } J_0(\delta_A) > 0 \\ \pi & \text{if } J_0(\delta_A) < 0 \end{cases}. \tag{6}$$

Combining Eqs. (5) and (6), the difference $\Delta\phi$ is

$$\Delta\phi = \begin{cases} 0 & \text{if } J_0(\delta_A) > 0 \\ \pi & \text{if } J_0(\delta_A) < 0 \\ \text{undefined} & \text{otherwise} \end{cases}. \tag{7}$$

Figure 2 illustrates the variation of $\Delta\phi$ with respect to $\overline{\delta_A}$, the absolute value of δ_A. Equation (7) shows that PSTA shearography only provides a binary phase pattern $\Delta\phi$, which is related to the amplitude of optical phase variation δ_A. The purpose of the current paper is to propose a method that estimates the map of vibration amplitudes φ_A (i.e., the vibration mode shape), related to δ_A through the following formula [4]:

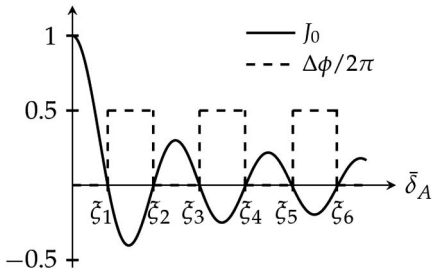

Fig. 2. Variation of phase differences $\Delta\phi$ with respect to the absolute values of directional displacements of vibration amplitudes in the shear direction ($\overline{\delta_A}$). The first six zeros ξ_k ($k = 1, \ldots, 6$) of the Bessel function J_0 are shown.

$$\delta_A = \frac{\partial \varphi_A}{\partial s}\Delta_s, \varphi_A = \frac{4\pi}{\lambda}\varphi, \tag{8}$$

where $\frac{\partial}{\partial s}$ is the directional derivative in the shear direction e_s and Δ_s is the shear displacement.

3. DESCRIPTION OF EXPERIMENTAL DATA

A. Data Acquired in Optics Laboratory

We acquired shearographic measurements of a metallic turbine blade. The blade base was clamped in a dedicated support attached to the stud of a shaker used to test the blade under vibration. The blade size (5 cm × 4 cm) is representative of the object sizes investigated in industrial environment. The shaker allows vibrations up to a few tens of kilohertz (kHz). The setup includes a continuous diode pumped laser at 532 nm wavelength (from company Coherent, model Verdi) and a CCD camera (from company Allied Vision, model Manta G 145) [27,28]. The final image size is 686 × 756 pixels out of the 1388 × 1038 available ones. Figure 3 shows the binary phase patterns $\Delta\phi$ acquired by shearography at resonance frequencies of 2910, 7960, 8450, and 8630 Hz, corresponding, respectively, to columns 1, 2, 3, and 4. The rows (a), (b), and (c) of Fig. 3 correspond to shear directions, respectively, vertical, horizontal, and diagonal, all with a shear amount of 1 mm.

B. Data Acquired in Industrial Environment

We acquired data of a metallic turbine blade at V2i S.A. The equipment is the same as for the optics laboratory data, except that the laser is a LMX from Oxxius, emitting 300 mW at 532 nm. We also used a band-pass filter centered at that wavelength for rejecting spurious ambient light (laser line cleanup filter from Edmund Optics). The blade is about 5 cm × 10 cm in size and occupies a small region in the field of view, with a final image of 400 × 800 pixels or 430 × 450 pixels (depending on the vibration setting) out of the 1280 × 1024 available ones. The shaker allows vibrations up to a few kHz, and the frequencies of the acquisitions are in the range of [360,1350] Hz. This dataset permits testing the method in a range of frequencies lower than the one of an optics laboratory. Both datasets cover the resonance frequencies between about 0.1 and 10 kHz.

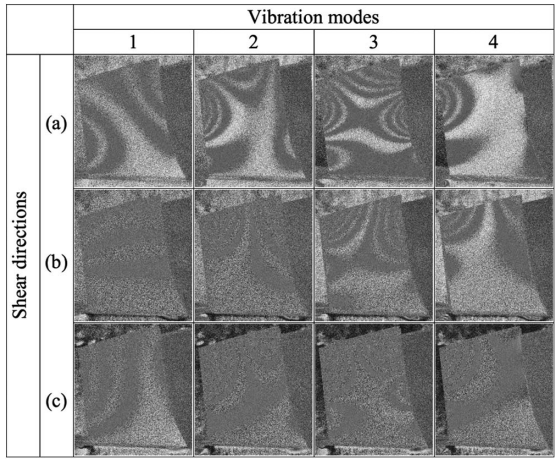

Fig. 3. Images of phase differences acquired by shearography at four resonance frequencies up to 10 kHz and for three shear directions.

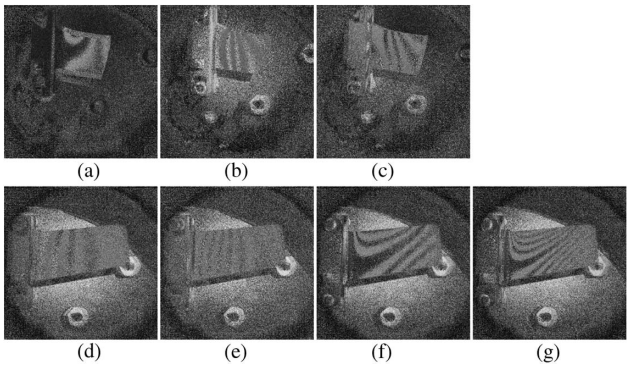

Fig. 4. Images of phase differences acquired by shearography at various resonance frequencies and shear settings. The frequencies are in the range [360,1350] Hz. The shear amplitude is 5 mm in (a) vertical and (b)–(g) horizontal directions.

Figure 4 shows images of phase differences acquired by shearography at various resonance frequencies and shear settings.

4. PRE-PROCESSING

The method we propose for estimating the map of vibration amplitudes from shearographic measurements is based on accurate delineation of the fringes in the original acquisition. Because it is based on the speckle effect, shearography is subject to speckle noise inherently present in the images (see in particular Fig. 4). The presence of speckle is related to object roughness [30]. Speckle grains have dimensions that depend on aperture of the imaging system [3]. In our results, a speckle represents 3–5 pixels. Another phenomenon can be seen in some figures of Fig. 4: the phases are not necessarily well defined (with values of 0 and π, seen as black and white fringes, like in Fig. 3) and can be shifted by a constant providing light gray and dark gray fringes. This is probably related to a bad application of phase-stepping in the industrial environment, and this does not help us to clearly, qualitatively observe the mode shape. This was already discussed in our previous paper [28]. Therefore, pre-processing is required for rotating the phases and attenuating the noise contained in shearographic observations.

A. Phase Rotation and Denoising

Now, we work in a discrete framework. The two-dimensional images of size $n_1 \times n_2$ are vectorized and belong to $\mathbb{R}^N$, where $N = n_1 n_2$. Pixel intensities of images are in $[0, 2\pi[$. We denote the 2π-modulo operator by $\mathcal{M}_{2\pi}$. Let $\Delta\phi \in \mathbb{R}^N$ be the original image of phase differences. We only have access to observations $z \in \mathbb{R}^N$, a wrapped and noisy version of $\Delta\phi$, which can be expressed as follows:

$$z = \mathcal{M}_{2\pi}(\Delta\phi + n), \tag{9}$$

where $\Delta\phi$ can only take values in $\{\Delta\phi_0, \Delta\phi_0 + \pi\}$ [see Eq. (7)], and $n \in \mathbb{R}^N$ is an additive Gaussian noise, where each n_i follows a Gaussian distribution of zero mean and variance σ_n^2.

Pre-processing looks for a good estimate $\Delta\phi_p \in \mathbb{R}^N$ for $\Delta\phi$ based on observations z. This stage is divided into two steps: *phase rotation* and *denoising*. We consider two denoising techniques. The first one is an adaptation of the well-known median filtering to phase images (MF). The second one is based on the resolution of an inverse problem enforcing the estimate to be piecewise constant, i.e., to have a small total variation (TV) [37].

1. Phase Rotation

Theoretically, the pixel intensities of fringes should only be 0 or π. Translating (or rotating on the circle $[0, 2\pi[$) the two peaks of the histogram to $\pi/2$ and $3\pi/2$ minimizes the noise outliers resulting from phase-wrapping in regions of lower and higher intensities (see right tail of noise distribution in Fig. 5). The histograms of pixel intensities inside the blade (selected with the blade mask M_b) show, however, initial distributions with two peaks located at $\Delta\phi_0$ and $\Delta\phi_0 + \pi$.

The first step of pre-processing is consequently applying the following phase rotation to the pixel values of z,

$$z_r = \mathcal{M}_{2\pi}(z - \Delta\phi_0 + \pi/2). \tag{10}$$

2. Denoising with Median Filter

The common way for removing noise in images of phase fringe patterns is applying a sine/cosine average filter [31]. The application of this principle is introduced in our context as follows. Filtering z_r with a linear filter, such as an average or Gaussian filter, would smooth the 2π discontinuities due to the wrapping operator. This problem is solved by calculating the sine and the cosine of z_r, which leads to the continuous fringe patterns $\sin z_r$ and $\cos z_r$. These patterns are then individually filtered, and the filtered version of z_r is obtained by applying successively the operators $\tan^{-1}$ and $\mathcal{M}_{2\pi}$. Such a filtering process is called sine/cosine filtering. For a filter operator F, its application on z_r leads to the estimate $\Delta\phi_p$, defined as

$$\Delta\phi_p = \mathcal{M}_{2\pi}(\tan^{-1}(F(\sin z_r)/F(\cos z_r))). \tag{11}$$

The median filter M_f is a nonlinear filter [32]. Its application on z_r is defined at pixel i as

$$[M_f(z_r)]_i = \text{Median}\{(z_r)_j | j \in W_\alpha(i)\}, \tag{12}$$

where $W_\alpha(i)$ is a square window of width α centered at pixel i.

This nonlinear filtering is more effective than linear filters for preserving edges and reducing impulse noise [33,34]. In this paper, we consider a sine/cosine median filter, for which the operator F in Eq. (11) is M_f.

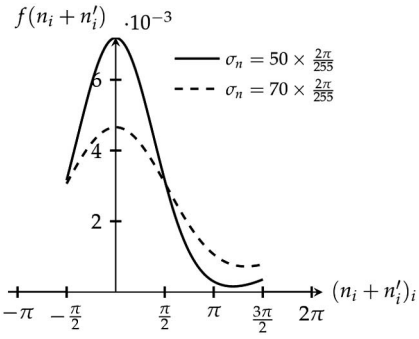

Fig. 5. Theoretical probability density function (pdf) of the additive noise $(n_i + n_i')$ on pixel i with intensity $(\Delta\phi_r)_i = \pi/2$. The pdf is represented for two different standard deviations σ_n.

3. Denoising via Regularized Inverse Problem Formulation

Filtering is useful in denoising images when only corrupted observations are available. However, extra knowledge about the acquisition model, the smoothness properties of the pure image, or the noise statistics allows us to formulate the denoising problem as an inverse problem. Such a problem aims at reversing the corruption process from the observations.

Forward Model: A key element in inverse problem resolution is to have an appropriate mathematical expression for the forward model, i.e., the model relating the observations to the original data. In our case, based on the knowledge of the ideal acquisition process (see Section 2) and on visual inspection of the histograms of experimental observations, the forward model can be described in first approximation as Eq. (9).

We will work with the equivalent equation for rotated observations defined by Eq. (10),

$$z_r = \mathcal{M}_{2\pi}(\Delta\phi_r + n), \tag{13}$$

where $\Delta\phi_r = (\Delta\phi - \Delta\phi_0 + \pi/2)$ can only take values in $\{\pi/2, 3\pi/2\}$. Equation (13) can be approximated as follows:

$$z_r \approx \Delta\phi_r + n + n' \in [0, 2\pi[\tag{14}$$

with an additive noise $n' \in \mathbb{R}^N$, where n'_i is distributed according to the following distribution knowing $(\Delta\phi_r)_i$:

$$n'_i = \begin{cases} 0 & \text{w.p. } p_0 = \mathbb{P}(-(\Delta\phi_r)_i \le n_i \le 2\pi - (\Delta\phi_r)_i), \\ -2\pi, & \text{w.p. } p_1 = \mathbb{P}(n_i > 2\pi - (\Delta\phi_r)_i), \\ 2\pi & \text{w.p. } p_2 = \mathbb{P}(n_i < -(\Delta\phi_r)_i), \end{cases} \tag{15}$$

where w.p. means *with probability*, and $\mathbb{P}$ is the probability symbol. In other words, the modulo operator is replaced by an impulse noise having the same effect on the data. Probabilities p_0, p_1, and p_2 depend on the variance σ_n^2 and on the values of $\Delta\phi_r$.

We are not interested in the exact knowledge of the distribution of n'_i, but rather in the shape and decay of this distribution (see Fig. 5 for theoretical distribution $f(n_i + n'_i)$).

Principle: The estimate of the original and noiseless image is computed via the resolution of the following minimization:

$$\Delta\phi_p = \arg\min_{x\in\mathbb{R}^N} \|x - z_r\|_1 + \alpha\Phi(x) \text{ subject to } x \ge 0, \tag{16}$$

where the first and second terms are called the *data fidelity term* and the *regularization term*, respectively. The ℓ_1-norm is defined as $\|x\|_1 = \sum_{i=1}^N |x_i|$ for $x \in \mathbb{R}^N$. This norm is well adapted for data corrupted by noise with outliers or by impulse noise, namely noise with heavy-tailed distribution [35,36]. We observe this behavior in shearographic measurements when the noise level is high (see Fig. 5). The regularization term $\Phi(x)$ stabilizes the inverse problem, initially ill-posed, by adding *a priori* knowledge to $\Delta\phi_p$. Parameter $\alpha > 0$ can be considered as a parameter making the trade-off between the two terms.

After application of the initial phase rotation, the binary phase maps have intensities equal to $\pi/2$ or $3\pi/2$, which are separated by smooth delineation curves. Therefore, the natural regularizing term Φ is the TV norm, which is minimal for cartoon-like images [37]. TV of an image $x \in \mathbb{R}^N$ is defined as the ℓ_1-norm of its gradient magnitude,

$$\Phi_{\mathrm{TV}}(x) = \|\|\nabla x\|_2\|_1 = \sum_{i=1}^N \|(\nabla x)_i\|_2, \tag{17}$$

where $\|\cdot\|_2$ denotes the ℓ_2-norm. The symbol ∇ represents the discrete gradient operator, defined as

$$\nabla : \mathbb{R}^N \to \mathbb{R}^{2N}, \qquad x \mapsto (\nabla x) = (\nabla_1 x^T, \nabla_2 x^T)^T, \tag{18}$$

where $\nabla_i \in \mathbb{R}^{N\times N}$ is the first spatial derivative along direction e_i, approximated numerically by first-order finite differences.

Implementation: For numerical implementation, Eq. (16) can be rewritten as an unconstrained minimization problem,

$$\Delta\phi_p = \arg\min_{x\in\mathbb{R}^N} \|x - z_r\|_1 + \alpha\Phi(x) + \iota_{\mathbb{R}_+^N}(x), \tag{19}$$

where indicator function $\iota_{\mathbb{R}_+^N}$ equals zero if x is non-negative and $+\infty$ otherwise. Optimal parameter α is such that $\|\Delta\phi_r - z_r\|_1 = \|\Delta\phi_p - z_r\|_1$, i.e., the ℓ_1-norms of noise and residual after denoising are equal. This optimal value is approximated by $\hat{\alpha}$, a parameter computed iteratively as follows. First, an (under)estimation of the noise ℓ_1-norm $\hat{n}_{\ell_1}$ is computed via fast MF denoising of z_r with a window width equal to 3. We choose a large initial value for $\hat{\alpha}$. Estimated that $\hat{\alpha}$ is updated after each denoising step according to the following rule:

$$\hat{\alpha}^{(k+1)} = \hat{\alpha}^{(k)}(\hat{n}_{\ell_1}/\|\Delta\phi_p^{(k)} - z_r\|_1). \tag{20}$$

This rule is applied only if the multiplicative factor is smaller than 1. Although heuristic, this updating rule allows for an automatic choice of the regularization parameter and gives good results, both for MF and TV denoising (see Sections 4.B and 4.C).

The algorithm used to solve Eq. (19) is the Chambolle–Pock primal dual algorithm [36]. It belongs to the family of proximal algorithms based on the concept of proximal operator [38]. Such algorithms are able to solve convex problems with non-smooth and non-differentiable objective functions, like Eq. (19).

B. Performance Evaluation on Synthetic Data

This section (*i*) evaluates the performance and the limitations of the pre-processing on synthetic data, and (*ii*) compares the performances of both denoising techniques, i.e., MF and TV denoising.

1. Quality Criterion

The quality of $\Delta\phi_p$ and z compared to $\Delta\phi_r$ is measured through the signal-to-noise ratio (SNR) metric. We define the SNR between an original image x_1 and another image x_2 as $\mathrm{SNR}(x_1, x_2) = 10\log(\|x_2\|_2^2/\|x_2 - x_1\|_2^2)$.

2. Synthetic Data

We created synthetic phantoms of the size 512 × 512 with pixel values $[0, 2\pi[$ and consisting of artificial blades rotated by an angle of 30° (see Fig. 6). The pixel intensity of the fringes is in $\{\pi/2, 3\pi/2\}$. Fringes density corresponds to the number of fringes per distance unit, i.e., per pixel.

We evaluate the limitations of the method with respect to two parameters of the input data, namely the noise level and the fringes density. To this end, we generated observations with different fringes densities and noise levels according to Eq. (9). Standard deviation σ_n corresponds to the SNR in the range of

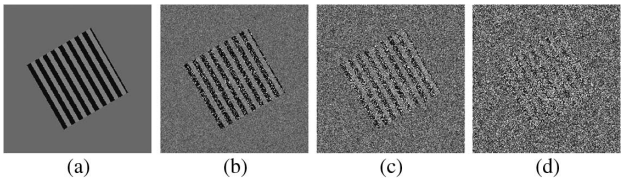

Fig. 6. Some of the synthetic observations z used for experiments described in Section 4.B.3 (fringes density is 0.06 and noise level varies from 5.3 to 7.6 dB). (a) Image $\Delta\phi$. (b) $\mathrm{SNR}_{\mathrm{in}} = 7.6$ dB. (c) $\mathrm{SNR}_{\mathrm{in}} = 6.4$ dB. (d) $\mathrm{SNR}_{\mathrm{in}} = 5.3$ dB.

5.3–7.6 dB (see Fig. 6), and the fringes density varies from 0.02 to 0.32. By comparison, the estimated SNR of experimental images acquired in an industrial environment (see Fig. 4) are between 6.7 and 9.9 dB. We estimate σ_n via the median absolute deviation (MAD) of the (high-pass) filtered blade pixels. The resulting estimate is $\hat{\sigma}_{\mathrm{MAD}} = 1.4826 \times \mathrm{MAD}(\text{blade pixels})$ [39].

3. Results and Discussion

We conducted the following simulations for MF and TV: (*i*) evaluating the quality of the output image for different levels of noise and fixed fringes density, and (*ii*) evaluating the quality of the output image for different fringes densities and fixed noise level.

Figure 7 shows the results of the first simulation, i.e., the mean SNR of estimate $\Delta\phi_p$ over 25 trials as a function of the SNR of observations z. The filled areas represent the standard deviation. The numbers near the nodes are the mean value of $\hat{\alpha}$ over all of the trials. For the highest level of noise, MF denoising leads to better results on average but with larger variations in SNR. Regarding the range of estimated SNR of experimental data acquired in an industrial environment, TV denoising should, however, give better results than MF denoising for real images.

Figure 8 illustrates the results of the second experiment for $\mathrm{SNR}_{\mathrm{in}} = 6.4$ dB. It shows that no matter the fringe density, TV denoising produces estimates $\Delta\phi_p$ with a higher SNR than MF denoising does. The difference of SNR is higher for images with only a few but large fringes. This behavior is similar for

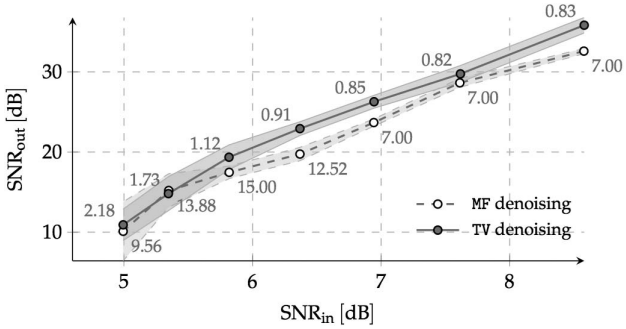

Fig. 7. Mean SNR (25 trials) of phase image estimate $\Delta\phi_p$ as a function of the SNR of z (fringes density: 0.06). Solid (respectively, dashed) line represents the mean value of $\mathrm{SNR}_{\mathrm{out}}$ obtained after TV (respectively, MF) denoising.

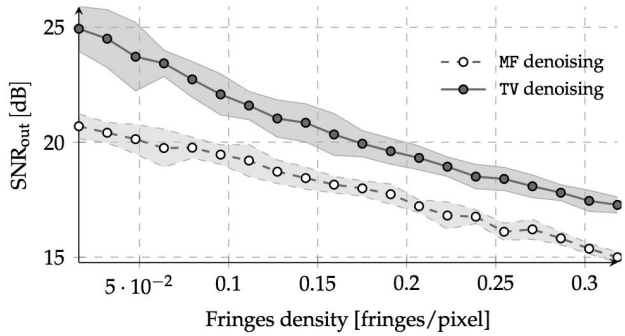

Fig. 8. Mean SNR (25 trials) of $\Delta\phi_p$ as a function of the fringes density of z ($\mathrm{SNR}_{\mathrm{in}} = 6.4$ dB). Solid (respectively, dashed) line represents the mean value of $\mathrm{SNR}_{\mathrm{out}}$ obtained after TV (respectively, MF) denoising.

higher values of $\mathrm{SNR}_{\mathrm{in}}$, including the range of $\mathrm{SNR}_{\mathrm{in}}$ estimated in the experimental data.

We conclude from synthetic experiments that TV denoising outperforms MF denoising for realistic noise levels. The larger the fringe densities are, the better TV denoising works compared to the MF technique. This result is not surprising, since TV denoising takes into account a structural prior on the image, while MF acts rather locally.

C. Qualitative Performance Based on Experimental Data

1. Quality Criterion

Due to multiple reasons (the lack of original data, the sparsity of experimental data in terms of fringe density and noise level), we are only able to qualitatively evaluate the denoising techniques by using a visual criterion: their ability to restore distinct fringes.

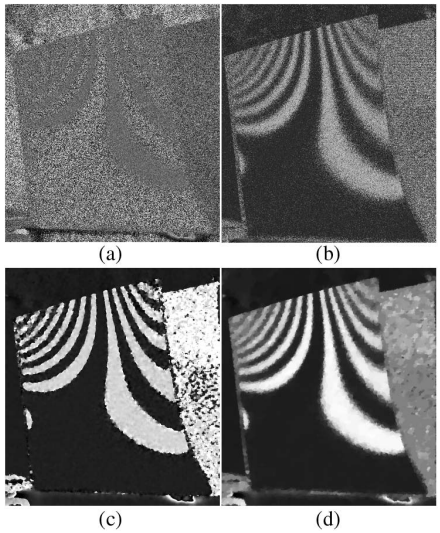

Fig. 9. Pre-processing results for the acquisition at vibration mode 2 in the horizontal shear direction. (a) z. (b) $\Delta\phi_r$. (c) $\Delta\phi_p$ after MF denoising. (d) $\Delta\phi_p$ after TV denoising.

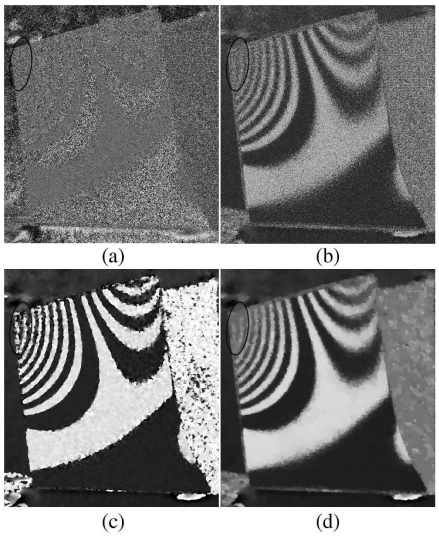

Fig. 10. Pre-processing results for the acquisition at vibration mode 2 in the diagonal shear direction. Black ellipses indicate areas where identification of fringes is difficult. (a) z. (b) $\Delta\phi_r$. (c) $\Delta\phi_p$ after MF denoising. (d) $\Delta\phi_p$ after TV denoising.

2. Results and Discussion

We pre-processed real data (from the optics laboratory and industrial environment) with both denoising techniques. As for synthetic data, all of the experiments were conducted with automatic selection of regularization parameter $\hat{\alpha}$.

Figures 9 and 10 show pre-processing results on two acquisitions from the optics laboratory. Pre-processing results on the acquisitions from the industrial environment with the highest fringe density [corresponding to Figs. 4(f) and 4(g)] are illustrated in Figs. 11 and 12.

Fringe identification is easier after pre-processing, even in areas where the fringes density is high. Figures 10 and 12 show examples, in which the identification of fringes in areas with high fringes remains difficult (see black ellipses).

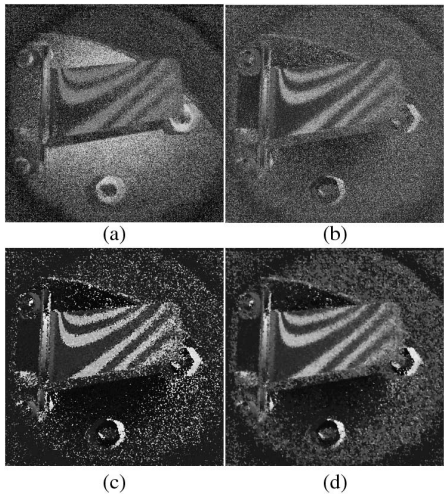

Fig. 11. Pre-processing results for acquisition of Fig. 4(f). (a) z. (b) $\Delta\phi_r$. (c) $\Delta\phi_p$ after MF denoising. (d) $\Delta\phi_p$ after TV denoising.

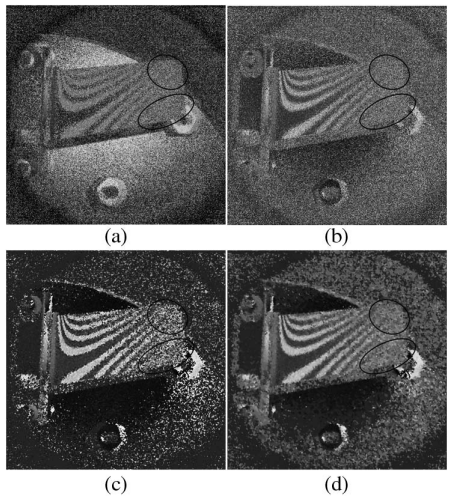

Fig. 12. Pre-processing results for acquisition of Fig. 4(g). Black ellipses indicate areas where identification of fringes is difficult. (a) z. (b) $\Delta\phi_r$. (c) $\Delta\phi_p$ after MF denoising. (d) $\Delta\phi_p$ after TV denoising.

5. PROCESSING: ESTIMATION OF VIBRATION AMPLITUDES

A. Overview

The (processing) method we propose for estimating the qualitative map of vibration amplitudes from shearographic measurements is based on a correct outlining of the fringes in the original acquisition. To limit the corruption due to the noise, we apply this method to the pre-processed image ($\Delta\phi_p$).

The method is based on the fact that the function of phase differences takes value 0 or π according to the sign of the Bessel function J_0 when the function $\overline{\delta_A}$ increases (see Fig. 2). Inside any fringe of $\Delta\phi_p$, the values of $\overline{\delta_A}$ vary between two zeros ξ_k, ξ_{k+1} of J_0. In the first approximation, we assume that $\overline{\delta_A}$ is constant inside any fringe of $\Delta\phi_p$, i.e., $\overline{\delta_A}$ is a piecewise constant function with sub-domains corresponding to the regions in which $\Delta\phi$ is constant (0 or π), i.e., in which $\Delta\phi_p$ takes the value $\pi/2$ or $3\pi/2$, after rotation in the pre-processing step (Section 4.A.1). In the context of TA speckle pattern interferometry, some techniques exist for providing a continuous phase from images of fringe patterns [15,17]. In Ref. [17], the technique is based on demodulation after approximation of the Bessel function J_0 by sinusoids. In Ref. [15], the technique is based on the inversion of the Bessel function J_0 and exists in two variants: a direct inversion and an optimization method.

We obtain the sub-domains of $\overline{\delta_A}$ by segmenting $\Delta\phi_p$ into the regions on which it is constant ($\pi/2$ or $3\pi/2$). Then, we build the function $\overline{\delta_A}$ by assigning a value to each of its sub-domains. The value is zero in the regions of zero-crossing (corresponding to vibration nodes) and is a zero value of the function J_0 in the other regions. A similar method used for indexing the intervals for the computed phases is described in Ref. [15].

There is insufficient information in the function $\overline{\delta_A}$ for directly estimating the function of vibration amplitudes φ_A. However, we can compute φ_A by integrating the function δ_A along the shear displacement,

$$\varphi_A = \int \delta_A \Delta_s \, ds, \qquad \delta_A = \overline{\delta_A}\,\mathrm{sign}(\delta_A). \tag{21}$$

The only missing information is the signs of δ_A. We estimate them in two steps. We first identify the regions of zero-crossing of δ_A, then, we estimate the signs of the displacements according to the number of regions of zero-crossing. One region of zero-crossing is *a priori* known: the clamped part of the blade that does not undergo relative movement with respect to the other part of the blade during the vibration. Therefore, we always assume that the vibration amplitude is zero at the clamping. If this region is the only region of zero-crossing, the sign of δ_A is constant in the other regions. We fix it at one. Otherwise, we assume that it alternates between the values −1 and 1 on both sides of the regions of zero-crossing.

We can exploit information both in the function $\Delta\phi_p$ of phase differences and in the image I_m redefined as

$$I_m = I_m J_0(\delta_A) \tag{22}$$

to automatically detect the regions of zero-crossing. Indeed, the fact that the Bessel function J_0 is maximum at zero (see Fig. 2) implies that the function I_m is maximum when δ_A is zero. Moreover, since I_m multiplies the sinusoidal functions in Eq. (4), the computation of ϕ from Eq. (6) makes the SNR of $\Delta\phi = \phi - \phi_r$ maximum. In conclusion, we can use the fact that the function I_m and the SNR of $\Delta\phi$ are maximum in regions of zero-crossing to detect them. In the remainder of the paper, we also call the newly defined I_m the *modulation intensity image*. Its computation from the four acquisitions obtained for the phase-shifting technique derives directly from Eq. (4):

$$I_m = \frac{1}{2}[(I_3 - I_1)^2 + (I_0 - I_2)^2]^{1/2}. \tag{23}$$

We finally obtain the function φ_A by integrating δ_A, a piecewise constant function, along the shear displacement. It results in a piecewise linear function φ_A. If this visual aspect prevents a good interpretation of the results, the method can improve it using mean-filtering. The resulting image is denoted as $\varphi_{A,s}$.

B. Processing Steps

Figure 13 shows the block diagram of the processing stage. The method requires the definition of the blade through a mask M_b equal to 1 inside the blade and zero in the background. Parameters a_m, p_e, T_m, Δ_s, and s_f are introduced in the following sections.

1. Binarization

The binarization (*i*) delineates the fringes of the denoised phases $\Delta\phi_p$ (obtained by pre-processing) via thresholding and (*ii*) cleans the regions of too small size using region-size filtering. The minimum area of the regions is determined by parameter a_m. The binarization step provides a binarized image $\Delta\phi_b$.

Thresholding: We convert $\Delta\phi_p$ into a binary image $\Delta\phi_b$ by setting the pixel values equal to 1 if the original values are larger than π and zero otherwise. We assume that the segments with a value of one correspond to fringes of $\Delta\phi_p$ for which the phase difference is $3\pi/2$, and that the segments with a value of zero correspond to fringes of $\Delta\phi_p$ for which the phase difference is $\pi/2$.

Region-size filtering: We remove regions with a size smaller than a percentage a_m of the area of the largest fringe (e.g., regions due to noise residuals). If the pixel intensities inside a region to suppress are equal to 1, they are set to zero and *vice versa*.

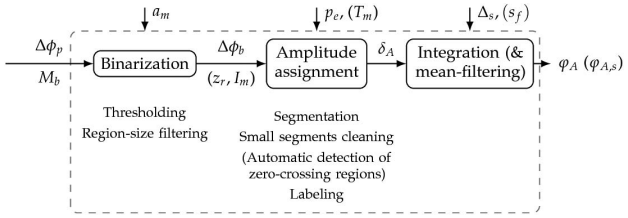

Fig. 13. Block diagram of the processing stage. Optional steps and their parameters are indicated in parenthesis.

2. Amplitude Assignment

The amplitude assignment builds the function δ_A by assigning a value to each region of $\Delta\phi_b$. It is divided into the following steps: segmentation, small-segments cleaning, possible automatic detection of zero-crossing regions, and labeling.

Segmentation: The segmentation divides the region defined by the blade mask into segments corresponding to the regions where $\Delta\phi_b$ is constant. The algorithm applied for delineating the segment boundaries is the Moore–Neighbor tracing algorithm using Jacob's stopping criterion [40]. The stages *small-segments cleaning* and *labeling* exploit the adjacency between segments. To make it possible, the segmentation also provides a table of adjacency strengths. We define the adjacency strength s_{kl} between two segments S_k, S_l as the number of pairs of pixels (p_k, p_l), such that p_k belongs to S_k, p_l belongs to S_l, and p_k is adjacent to p_l. With this definition, the adjacency strength between two non-adjacent segments is equal to 0. For a segmentation of N segments, we define the table of adjacency strengths as the table A of N^2 elements, with element $A(k,l)$ defined as

$$A(k,l) = \frac{s_{kl}}{\sum_l s_{kl}}, \qquad k,l = 0,\ldots,N-1. \tag{24}$$

Small-segments cleaning: Small-segments cleaning removes small holes caused by residual noise in the image $\Delta\phi_p$. Let us consider a segment S_k included in another segment S_l. This segment is small in comparison to S_l if its strength is smaller than 10% of the maximum strength among all strengths of segments adjacent to S_l. The adjacency table is used to locate such couples of segments (S_k, S_l). Indices k are the ones for which the row $A(k,l)$ has only one non-zero value. For each such index k, index l is the one of the non-zero elements $A(k,l)$. The adjacency table is also used to determine the strengths involved in the smallness condition.

Automatic detection of nodal lines: Among the nodal lines (or regions of zero-crossings Z_k), one region Z_0 is *a priori* known: the nodal line including the clamped part of the blade that is fixed during the vibration test. This zone can be easily identified by a point (parameter p_e). The automatic detection of the other nodal lines is based on the fact that the function I_m [see Eqs. (22) and (23)] and the SNR of z are maximum in such regions. The noise contained in the image I_m can lead

to insignificant local maxima generating artificial regions of zero-crossing. To prevent it, we first threshold I_m using a threshold (parameter T_m):

$$I_m = \begin{cases} I_m & \text{if } I_m > T_m \\ 0 & \text{otherwise} \end{cases}. \tag{25}$$

The process for identifying the regions Z_k starts by assigning to each segment S_k of the binarized image $\Delta\phi_b$ two values: *(i)* the standard deviation σ_{Z_k} of z inside S_k and *(ii)* the mean value m_{Z_k} of the image I_m inside S_k. These values are compared, and a segment S_k is identified as a nodal line (Z_k) if the two values σ_{Z_k} and m_{Z_k} assigned to S_k are higher than the values σ_{Z_l} and m_{Z_l} in its adjacent regions.

Labeling: Labeling assumes that each region of zero-crossing has only one or two adjacent regions. Without this assumption, the information contained in images z and I_m is insufficient to estimate the sign of δ_A. The acquisitions should be conducted so that the produced measurements fulfill this assumption. This requires tuning the vibration frequency accordingly. The labeling is performed in two steps: the estimation of $\overline{\delta_A}$ and the estimation of the signs of δ_A. The multiplication of the two resulting images provides an estimation of δ_A.

Estimation of $\overline{\delta_A}$ is made in two steps. First, we assign to each segment a null or positive integer n, representing the order of succession of the region counted from the regions Z_k of zero-crossing. This step is iterative: it starts by assigning the value zero to the regions Z_k, and then it operates iteratively using the adjacency table to process from each assigned region to its adjacent ones (by assigning the value $n+1$ to each adjacent region of a region with n value). During the second step, we replace each n value by the nth zero value of the Bessel function J_0.

The estimation of the signs of δ_A is made in three steps. First, we merge the set of segments that are not the regions Z_k of nodal lines. The resulting regions are indicated by M_k. Then, we assign the sign one to the region M_k that is closest to the region Z_0 (the one including the clamped part). If there is more than one region of zero-crossing, there is also more than one region M_k, and we assign to the other regions M_k the sign −1 or 1 by alternating between −1 and 1 on both sides of the regions Z_k.

3. Integration and Mean-Filtering

Integration is achieved using the simplest inverse operator of the directional displacement operator numerically approximated by finite differences. Let x indicate the function resulting from the integration of a displacement image d along vector Δ_s of coordinates $(\Delta_{s,1}, \Delta_{s,2})$ and of length $\overline{\Delta_s}$. The value of x at any pixel p of coordinates (p_1, p_2) is computed from its value and the value of d at pixel p' of coordinates $(p_1 - \Delta_{s,1}, p_2 - \Delta_{s,2})$:

$$x(p) = c(p) + x(p') + d(p'), \tag{26}$$

where function c is constant with respect to the integration direction. This latter function is initialized from the boundary conditions on the edges of the blade mask. The mean-filtering is a convolution with a square kernel of size s_f.

C. Real Data Experiment

1. Quality Criteria

A quantitative evaluation of processing would require the creation of synthetic maps of vibration amplitudes and the generation of shearographic measurements via time-consuming methods. Such a study has not been envisaged at this step, but could be performed in a future work. Instead, we qualitatively evaluated processing on real data by using some criteria of visual analysis. The criteria and their associated symbols are listed in Table 1.

When the criteria $\mathcal{Z}$ and $\mathcal{F}$ are fulfilled, the method detects all the fringes; it, thus, estimates suitably the image of absolute values of displacements ($\overline{\delta_A}$). When, in addition, criterion $\mathcal{L}$ is satisfied, the processing properly estimates the image of displacements (δ_A), and, after integration, it estimates appropriately the image of vibration amplitudes. In this case, the processing is working properly.

We applied the processing stage to each pre-processed image obtained for both denoising techniques, with the updated rule for computing the estimate $\hat{\alpha}$ of the optimal parameter α. Then, we selected the denoising technique providing the largest number of criteria in Table 1. When both results are equivalent, we select the one providing the least mergers of fringes and/or the less fragmented contours of fringes.

2. Results

Data from optics laboratory: We exploit data acquired in optics laboratory (*i*) to test the method for the most important vibration modes in strain tests (obtained at resonance frequencies below 10 kHz) and (*ii*) to evaluate the ability of our method to facilitate mode identification.

Table 2 lists, for each acquisition, the criteria of Table 1 fulfilled by the results. Eleven out of 12 acquisitions have their result satisfying criteria $\mathcal{Z}$ and $\mathcal{F}$, thus resulting with appropriate estimations of the image $\overline{\delta_A}$. In the last acquisition, the combination of a significant noise level (the same for all acquisitions) and a high fringes density makes the estimation of the image $\overline{\delta_A}$ difficult: the binarization produces merging of fringes.

Table 1. Criteria for Visual Analysis

Symbol	Criterion
$\mathcal{L}$	Fulfillment of the labeling assumption (see paragraph Labeling in Section 5.B.2)
$\mathcal{Z}$	Suitable detection of the regions of zero-crossing
$\mathcal{F}$	Suitable detection of other fringes (different from regions of zero-crossing)

Table 2. Criteria Fulfilled by the Best Result of Each Acquisition

	Vibration Modes			
Shear Direction	1	2	3	4
Vertical	$\mathcal{LZF}$	$\mathcal{ZF}$	$\mathcal{LZF}$	$\mathcal{ZF}$
Horizontal	$\mathcal{LZF}$	$\mathcal{LZF}$	$\mathcal{ZF}$	$\mathcal{ZF}$
Diagonal	$\mathcal{LZF}$	$\mathcal{LZ}$	$\mathcal{ZF}$	$\mathcal{LZF}$

Only half of the acquisitions satisfies criterion $\mathcal{L}$, providing a suitable estimation of the vibration amplitudes.

Two examples of results satisfying criteria $\mathcal{Z}$ and $\mathcal{F}$ are shown in Figs. 14 and 15. Figure 14 illustrates a proper working of the method: it shows a result satisfying criterion $\mathcal{L}$. Figure 15 shows a result not fulfilling the criterion $\mathcal{L}$. In these two examples, the region Z_0, including the clamped part, is the only region of zero-crossing. No other region of zero-crossing is detected, as shown in Figs. 14(d) and 15(d). Therefore, the criterion $\mathcal{Z}$ is fulfilled. Although the region Z_0 is not automatically detected by our method, our process of automatic detection of regions of zero-crossing is robust enough, since, as shown in Figs. 14(c) and 15(c), the intensity modulation image is maximum in Z_0. In the first example, the region Z_0 has only two adjacent regions so that the criterion $\mathcal{L}$ is fulfilled. In the second example, it has five adjacent regions so that the criterion $\mathcal{L}$ is not satisfied. In the two examples, no merging of fringes appears in the estimation of δ_A, so that criterion $\mathcal{F}$ is satisfied.

The single result not satisfying criterion $\mathcal{F}$ is shown in Fig. 16. The regions of zero-crossing are correctly identified according to the modulation intensity image [see Figs. 16(c) and 16(d)]. The incorrect detection of other fringes is due to mergers between fringes [see ellipses in Figs. 16(b) and 16(e)]. These mergers appear in regions where the fringes density is so high that the initial noise level prevents the distinction of fringes in the original image [see black ellipse in Fig. 10(a)]. Although denoising allows a better distinction between these fringes, it cannot completely separate them [see black ellipse in Fig. 16(a)].

In strain tests, non-experts can easily identify the vibration modes from ESPI acquisitions. The purpose of our method is to provide images from shearographic acquisitions that will help non-experts to identify the most important vibration modes in strain tests, i.e., modes obtained at the first four resonance frequencies below 10 kHz.

Since few acquisitions at the first four vibration modes satisfy criterion $\mathcal{L}$ (see Table 2), the vibration amplitude maps provided by integration of their displacement are not suitable for identifying vibration modes. Nevertheless, the images of their displacement maps are sufficient to that purpose, as shown in Fig. 17. Moreover, the shear direction perpendicular to the direction of the blade base is more appropriate for a better identification of vibration modes. In the current situation, where the blade is fixed from the bottom, the more suitable direction is the vertical one [see Fig. 17(a)].

Data from industrial environment: We exploit data acquired in an industrial environment to qualitatively assess the method in an environment less controlled than a laboratory.

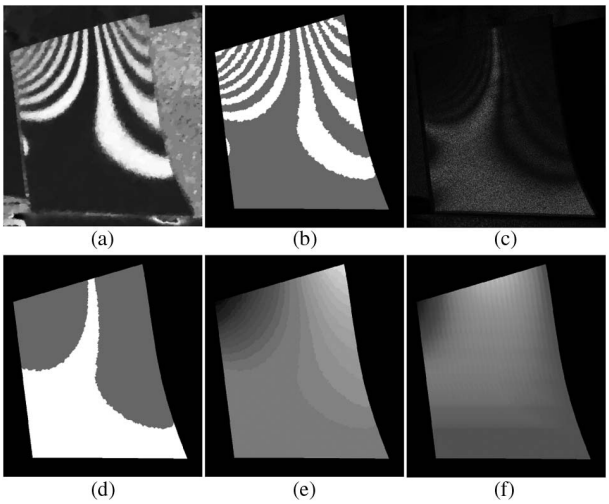

Fig. 14. Results for the acquisition at vibration mode 2 in the horizontal shear direction (after TV denoising). (a) $\Delta\phi_p$. (b) $\Delta\phi_b$. (c) I_m. (d) Regions Z_k. (e) Estimation of δ_A. (f) Estimation of ϕ_A.

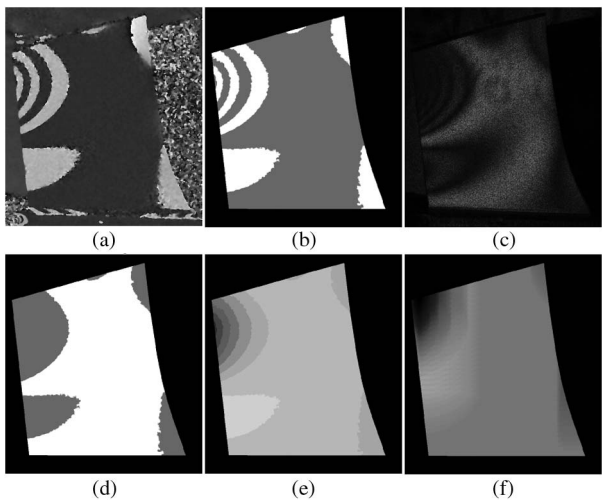

Fig. 15. Results for the acquisition at vibration mode 4 in the vertical shear direction (after MF denoising). (a) $\Delta\phi_p$. (b) $\Delta\phi_b$. (c) I_m. (d) Regions Z_k. (e) Estimation of δ_A. (f) Estimation of φ_A.

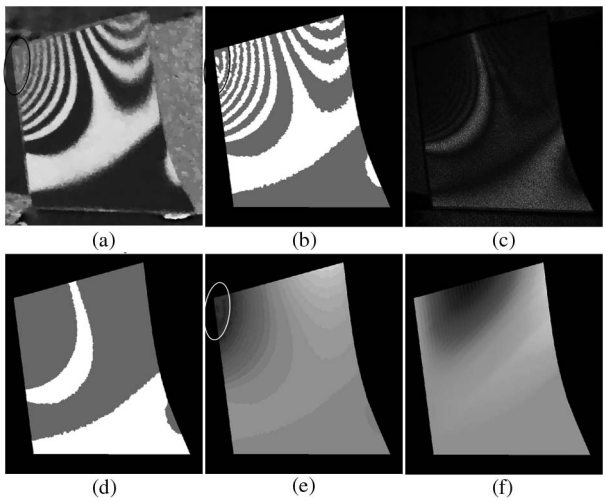

Fig. 16. Results for the acquisition at vibration mode 2 in the diagonal shear direction (after TV denoising). Ellipses indicate mergers of fringes. (a) $\Delta\phi_p$. (b) $\Delta\phi_b$. (c) I_m. (d) Regions Z_k. (e) Estimation of δ_A. (f) Estimation of φ_A.

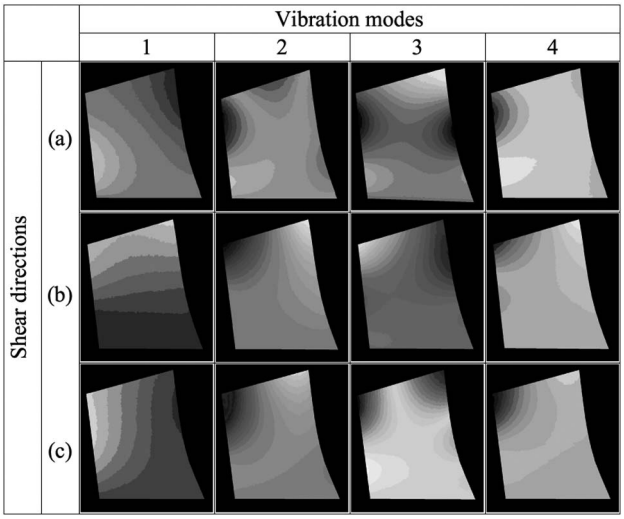

Fig. 17. Images of displacements estimated from shearographic acquisitions at the first four vibration modes. Shear directions are (a) vertical, (b) horizontal, and (c) diagonal.

Table 3. Criteria Fulfilled by the Best Result of Each Acquisition

Image (as part of Fig. 4)	Criterion
(a)–(f)	$\mathcal{LZF}$
(g)	—

Table 3 lists, for each acquisition, the criteria of Table 1 that are fulfilled by the results. Almost all of the acquisitions (six out of seven) have their result satisfying all the criteria obtained by a proper working of the processing. In the remaining acquisition [see Fig. 4(g)], the combination of the significant noise level and a too high fringes density involves the merging of fringes after binarization. The latter prevents the correct detection of regions of zero-crossing and the suitable estimation of image $\overline{\delta_A}$.

Figure 18 illustrates a proper working of the processing, i.e., images fulfilling criteria $\mathcal{L}$, $\mathcal{Z}$, and $\mathcal{F}$, on the acquisition with the highest fringes density [see Fig. 4(f)]. In this example, the region Z_0, including the clamped part, is the only region of zero-crossing. No other region of zero-crossing is detected, as shown in Fig. 18(d). Therefore, criterion $\mathcal{Z}$ is satisfied. The region Z_0 has only two adjacent regions so that criterion $\mathcal{L}$ is fulfilled. Finally, no merging of fringes appears in the estimation of δ_A, so that criterion $\mathcal{F}$ is satisfied. The fulfillment of all criteria allows a suitable estimation of the vibration amplitudes through the integration, as shown in Fig. 18(f).

The single unsatisfactory result is shown in Fig. 19. The incorrect detection of the regions of zero-crossing and the other fringes are due to mergers between fringes [see black ellipses in Figs. 19(d) and 19(e)]. These mergers appear in regions where the fringes density is very high. The remaining noise after denoising prevents the complete distinction between the fringes [see black ellipses in Fig. 19(a)].

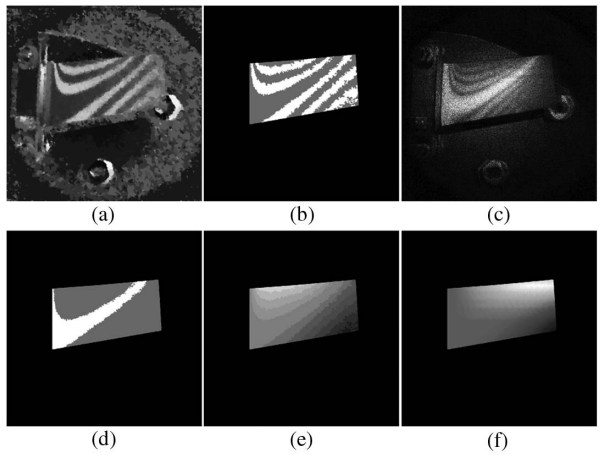

Fig. 18. Best result for image of Fig. 4(f) (after TV denoising). (a) $\Delta\phi_p$. (b) $\Delta\phi_b$. (c) I_m. (d) Regions Z_k. (e) Estimation of δ_A. (f) Estimation of φ_A.

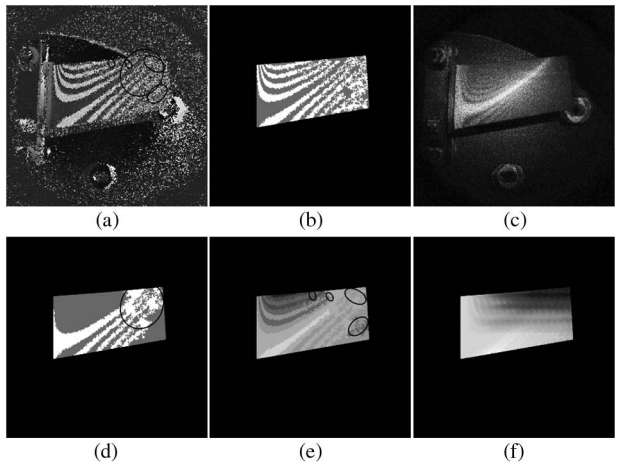

Fig. 19. Best result for image of Fig. 4(g) (after MF denoising). Ellipses indicate mergers of fringes. (a) $\Delta\phi_p$. (b) $\Delta\phi_b$. (c) I_m. (d) Regions Z_k. (e) Estimation of δ_A. (f) Estimation of φ_A.

3. Discussion

The application of processing on data acquired in an optics laboratory shows that almost all acquisitions provide results with appropriate estimation of the image of the displacements of vibration amplitudes and that these estimations are enough for identifying most of the important vibration modes in strain tests, i.e., modes obtained at resonance frequencies below 10 kHz. It also shows that shear direction perpendicular to the direction of the blade base is more appropriate for a better identification of these vibration modes.

Such analysis would be interesting for vibration modes at frequencies higher than 10 kHz. However, acquiring data at such vibration frequencies will unavoidably lead to images containing high fringes density. However, the combination of high initial fringes density with a noise level that is representative of real acquisition conditions prevents a correct identification of the original fringes from the pre-processed image. This alters

the good working of the processing, which provides inaccurate vibration maps that prevent a correct identification of the original vibration modes. Future work could be the improvement of the robustness against noise so that the presence of high fringes density disrupts the delineating of the fringes boundaries as little as possible. Robustness against noise could be considered in pre-processing and in the *segmentation* part of processing.

Data acquired in an industrial environment were obtained for vibrations in a range of frequencies lower than the one of an optics laboratory. The application of processing on this dataset shows that all acquisitions but one provide results with appropriate estimation of the image of vibration amplitudes. Actually, these results illustrate the limits of the method with respect to two acquisition parameters: the noise level and the fringes density. For all acquisitions but one, these parameters are in an adequate range so that processing provides images of vibration amplitudes of good quality and that are suitable for interpretation by non-experts. On the other acquisition, the fringes density is too high for correctly identifying the original fringes from the pre-processed image.

6. CONCLUSION

Shearography is a contactless optical technique used for vibration analysis. Non-experts in this field can easily interpret the vibration measurements if they have access to the amplitude of vibration mode shapes. However, shearography does not provide it directly, but rather it provides the phase differences related to the derivative of displacements. Moreover, in our case, we use a very simple method based on phase-shifting applied in the TA mode. This allows one to rapidly obtain binary phase fringe patterns with better contrast and resolution compared to other techniques based on TA, in particular, when they are applied in industrial environments where noise can become important in the images. In this paper, we proposed a method for estimating the vibration amplitudes from shearographic measurements under the PSTA method, tackling the effect of different noise sources that are present in the experimental data. The method is divided into two stages: pre-processing and processing. The main goal of pre-processing is to reduce the noise contained in the shearographic acquisitions. We considered two denoising techniques. The processing stage, including spatial integration, provides a map of vibration amplitudes from a less noisy estimation of the initial image (the pre-processed image). Experiments on synthetic data revealed that TV denoising outperforms MF denoising in terms of noise reduction, especially for large fringes densities. Experiments on real data show that, for almost all acquisitions, the noise level and the fringes density are in an adequate range for delivering images of vibration amplitudes of good quality suitable for interpretation by non-experts. In addition, experiments on data acquired in an optics laboratory show the adequacy of the proposed method for identifying vibration modes.

Future work concerns three parts of the work: pre-processing, processing, and evaluation of the entire method. In pre-processing, we could choose a better regularizer Φ. TV acts only locally and can lead to non-smooth fringes delineation (known as the staircasing effect). To circumvent this in a future work, we could use a regularization term enforcing sparsity of the image in the curvelet domain [41] or denoise $\mathbb{S}^1$ intensity valued images (with $\mathbb{S}^1$ as the periodic circle) instead of estimating the impact of the wrapping operator [42]. Concerning processing, the mean filtering could be avoided by looking for a solution where δ_A is more regular than a piecewise constant function, e.g., by assigning values interpolated between the zeros of the zeroth-order Bessel function of first kind to the fringes of the pre-processed image. A technique similar to the one described in Ref. [15] for providing a phase map as a continuous solution to the inversion of the Bessel function J_0 could be adapted to our context for providing a continuous map of amplitudes of optical phase variation δ_A. Moreover, integration is chosen among the techniques for inverting the directional displacement operator as the simplest one. In a future work, we could implement a better technique by solving an optimization problem under regularization. Besides providing results less sensitive to initial noise variation, this would improve their visual aspect without need of post-processing such as mean filtering. The evaluation of the entire method could be improved by the addition of quantitative evaluation of processing and assessment of the correct identification of vibration modes at frequencies higher than 10 kHz.

Funding. Wallonia DG06 (6894); Fonds De La Recherche Scientifique - FNRS (FNRS); AlterSense (MIS-FNRS).

Acknowledgment. The study presented in this paper has been achieved in the AOC project funded by Wallonia DG06 (contract 6894). L. Jacques is funded by the FNRS. Part of this study was funded by the project AlterSense (MIS-FNRS). The authors would like to pay tribute to Prof. Dan Borza († May 26 2018), inventor of the PSTA method used in this work.

REFERENCES

1. T. Kreis, *Holographic Interferometry* (Wiley-VCH Verlag GmbH & Co. KGaA, 2005).
2. P. Picart, M. Gross, and P. Marquet, "Basic fundamentals of digital holography," in *New Techniques in Digital Holography*, P. Picart, ed. (Wiley-ISTE, 2015).
3. A. E. Ennos, "Speckle interferometry," in *Laser Speckle and Related Phenomena*, J. C. Dainty, ed., 2nd ed. (Springer, 1984).
4. W. Steinchen and L. Yang, *Digital Shearography: Theory and Application of Digital Speckle Pattern Shearing Interferometry* (SPIE, 2003).
5. M. K. Kalms and W. Osten, "Mobile shearography system for the inspection of aircraft and automotive components," Opt. Eng. **42**, 1188–1196 (2003).
6. D. Francis, R. P. Tatam, and R. M. Groves, "Shearography technology and applications: a review," Meas. Sci. Technol. **21**, 102001 (2010).
7. M. R. Viotti and A. Albertazzi, Jr., *Robust Speckle Metrology: Techniques for Stress Analysis and NDT* (SPIE, 2014).
8. R. Powell and K. A. Stetson, "Interferometric vibration analysis by wavefront reconstruction," J. Opt. Soc. Am. **55**, 1593–1598 (1965).
9. K. Creath and G. Å. Slettemoen, "Vibration-observation techniques for digital speckle-pattern interferometry," J. Opt. Soc. Am. A **2**, 1629–1636 (1985).
10. E. Vikhagen, "Vibration measurement using phase shifting TV-holography and digital image processing," Opt. Commun. **69**, 214–218 (1989).
11. O. J. Lokberg and K. Hogmoen, "Use of modulated reference wave in electronic speckle pattern interferometry," J. Phys. E **9**, 847–851 (1976).

12. K. A. Stetson and W. R. Brohinski, "Fringe-shifting technique for numerical analysis of time-average holograms of vibrating objects," J. Opt. Soc. Am. A **5**, 1472–1476 (1988).
13. S. Ellingsrud and G. O. Rosvold, "Analysis of data-based TV-holography system used to measure small vibration amplitudes," J. Opt. Soc. Am. A **9**, 237–251 (1992).
14. U. P. Kumar, Y. Kalyani, N. K. Mohan, and M. P. Kothiyal, "Time-average TV holography for vibration fringe analysis," Appl. Opt. **48**, 3094–3101 (2009).
15. T. Statsenko, V. Chatziioannou, T. Moore, and W. Kausel, "Methods of phase reconstruction for time-averaging electronic speckle pattern interferometry," Appl. Opt. **55**, 1913–1919 (2016).
16. T. Statsenko, V. Chatziioannou, T. Moore, and W. Kausel, "Deformation reconstruction by means of surface optimization. Part I: time-averaged electronic speckle pattern interferometry," Appl. Opt. **56**, 654–661 (2017).
17. B. Deepan, C. Quan, and C. J. Tay, "Quantitative vibration analysis using a single fringe pattern in time-average speckle interferometry," Appl. Opt. **55**, 5876–5883 (2016).
18. A. Styk and M. Brzezinski, "Vibration amplitude recovery from time averaged interferograms using the directional spatial carrier phase shifting method," Proc. SPIE **8082**, 80821X (2011).
19. U. P. Kumar, N. K. Mohan, and M. P. Kothiyal, "Time average vibration fringe analysis using Hilbert transformation," Appl. Opt. **49**, 5777–5786 (2010).
20. M. Wielgus and K. Patorski, "Evaluation of amplitude encoded fringe patterns using the bidimensional empirical mode decomposition and the 2D Hilbert transform generalizations," Appl. Opt. **50**, 5513–5523 (2011).
21. M. Trusiak, A. Styk, and K. Patorski, "Hilbert–Huang transform based advanced Bessel fringe generation and demodulation for full-field vibration studies of specular reflection micro-objects," Opt. Lasers Eng. **110**, 100–112 (2018).
22. L. Yang, W. Steinchen, G. Kupfer, P. Mäckel, and F. Vössing, "Vibration analysis by means of digital shearography," Opt. Lasers Eng. **30**, 199–212 (1998).
23. S. Nakadate, H. Saito, and T. Nakajima, "Vibration measurement using phase-shifting stroboscopic holographic interferometry," Opt. Acta **33**, 1295–1309 (1986).
24. D. N. Borza, "Full-field vibration amplitude recovery from high-resolution time-averaged speckle interferograms and digital holograms by regional inverting of the Bessel function," Opt. Lasers Eng. **44**, 747–770 (2006).
25. D. Borza, "High-resolution time-average electronic holography for vibration measurement," Opt. Lasers Eng. **41**, 515–527 (2004).
26. D. N. Borza, "A new interferometric method for vibration measurement by electronic holography," Exp. Mech. **42**, 432–438 (2002).
27. J.-F. Vandenrijt, C. Thizy, and M. P. Georges, "Vibration analysis by speckle interferometry with CO_2 lasers and microbolometers arrays," in *Imaging and Applied Optics* (2014), paper DTh4B.8.
28. F. Languy, J.-F. Vandenrijt, and C. Thizy, J. Rochet and C. Loffet, D. Simon and M. P. Georges, "Vibration mode shapes visualization in industrial environment by real-time time-averaged phase-stepped electronic speckle pattern interferometry at 10.6 μm and shearography at 532 nm," Opt. Eng. **55**, 121704 (2016).
29. K. Creath, "Phase-measurement interferometry techniques," Prog. Opt. **26**, 349–393 (1988).
30. I. Yamaguchi, "Fundamentals and applications of speckle," Proc. SPIE **4933**, 1–8 (2003).
31. H. Aebischer and S. Waldner, "Simple and effective method for filtering speckle-interferometric phase fringe patterns," Opt. Commun. **162**, 205–210 (1999).
32. T. Bose, *Digital Signal and Image Processing* (Utah State University, Wiley, 2004).
33. I. Pitas and A. N. Venetsanopoulos, *Nonlinear Digital Filters: Principles and Applications* (Kluwer Academic, 1990).
34. A. C. Bovik, T. S. Huang, and J. D. C. Munson, "The effect of median filtering on edge estimation and detection," IEEE Trans. Pattern Anal. Mach. Intell. **PAMI-9**, 181–194 (1987).
35. M. Nikolova, "A variational approach to remove outliers and impulse noise," J. Math. Imaging Vis. **20**, 99–120 (2004).
36. A. Chambolle and T. Pock, "A first-order primal-dual algorithm for convex problems with applications to imaging," J. Math. Imaging Vis. **40**, 120–145 (2011).
37. L. I. Rudin, S. Osher, and E. Fatemi, "Nonlinear total variation based noise removal algorithms," Physica D **60**, 259–268 (1992).
38. N. Parikh and S. Boyd, "Proximal algorithms," in *Foundations and Trends in Optimization* (2014), Vol. **1**, pp. 127–239.
39. L. Sachs, *Applied Statistics: A Handbook of Techniques*, 2nd ed. (Springer, 1984).
40. R. C. Gonzalez, R. E. Woods, and S. L. Eddins, *Digital Image Processing Using MATLAB* (Prentice Hall, 2004).
41. J.-L. Starck, E. J. Candes, and D. L. Donoho, "The curvelet transform for image denoising," IEEE Trans. Image Process. **11**, 670–684 (2002).
42. R. Bergmann, F. Laus, G. Steidl, and A. Weinmann, "Second order differences of cyclic data and applications in variational denoising," SIAM J. Imaging Sci. **7**, 2916–2953 (2014).